Correlations between morphology, crystal structure and magnetization of epitaxial cobalt-platinum films grown with pulsed laser ablation

R. K. Rakshit, S. K. Bose, R. Sharma and R. C. Budhani[a]

Condensed Matter - Low Dimensional Systems Laboratory, Department of Physics,

Indian Institute of Technology Kanpur, Kanpur - 208 016, India

T. Vijaykumar, S. J. Neena and G. U. Kulkarni

Jawaharlal Nehru Centre for Advanced Scientific Research,

Jakkur P.O., Bangalore 560 064, India

Abstract

The effects of growth rate (G_r), deposition temperature (T_d), film thickness (t_F), and substrate induced strain (ϵ) on morphological, crystallographic and magnetic characteristics of equiatomic CoPt epitaxial films synthesized with pulsed laser deposition (PLD) are investigated. The (001) oriented single crystal substrates of MgO, $SrTiO_3$ and $LaAlO_3$ provide different degree of epitaxial strain for growth of the disordered face centered cubic (fcc) and ordered face centered tetragonal ($L1_0$) phases of CoPt. The films deposited at $T_d \approx 600\ ^0$C on all three substrates are fcc with in-plane magnetization and a narrow hysteresis loop of width ≈ 200 Oe. The $L1_0$ phase, stabilized only at $T_d \geq 700\ ^0$C becomes predominantly c-axis oriented as T_d is increased to $800\ ^0$C. While the crystallographic structure of the films depends solely on the T_d, their microstructure and magnetization characteristics are decided by the growth rate. At the higher G_r (≈ 1 Å/sec) the $L1_0$ films have a maze-like structure which converts to a continuous film as the t_F is increased from 20 nm to 50 nm. The magnetic coercivity of these films increases as the $L1_0$ phase fraction grows with T_d and its orientation becomes out of the film plane. The evolution of microstructure with T_d is remarkably different at lower growth rate (≈ 0.4 Å/sec). Here the structure changes from a self-similar fractal pattern to a disordered assembly of nano-dots as the T_d is raised from

700 to 800 ^{0}C, and is understood in terms of the imbalance between strain and interfacial energies. Magnetic force microscopy of such films reveals no distinct domain walls within the nano-islands while a clear contrast is seen between the islands of reversed magnetization. Magnetic relaxation measurements on these assemblies of single-domain islands show negligible decay of magnetization unless a reverse field close to the coercive field ($H_c \approx 30$ kOe) is applied. The simple picture of coherent rotation of moment appears incompatible with the time dependence of the remanent magnetization in these films.

[a] Author to whom correspondence should be addressed; electronic mail: rcb@iitk.ac.in

I. INTRODUCTION

Studies of the correlations between crystallographic as well as morphological structure and magnetic coercivity of CoPt and FePt alloy films have been of considerable interest in recent years due to the strong perpendicular magnetic anisotropy and chemical inertness of these alloys which make them suitable for high density recording applications[1,2,3,4,5,6,7,8,9,10,11,12,13,14,15,16,17]. The key structural feature responsible for magnetic anisotropy of these systems is the ordering of Pt and Co or Fe atoms in the crystal lattice. The ordered $L1_0$ phase at equiatomic composition comprises of an alternate sequence of Co (Fe) and Pt planes along the crystallographic c-axis[18]. Studies of coercivity and magnetization reversal in granular thin films of CoPt and FePt are of interest as well. When the size of grains becomes small enough to make them mono-domain, the magnetic response of the system may differ significantly from that in the bulk form. Studies of thermal stability of magnetization and the process of its reversal are critical for high density recording. The reversal can occur either continuously through coherent or incoherent rotation of spins, or discontinuously through nucleation of reversed domains and their expansion through domain wall displacement[19,20]. Growth of reverse domains can be impeded by defects, such

as second-phase precipitates or grain boundaries which pin the domain walls by locally altering their energy. In epitaxial films consisting of discontinuous islands/dots of sufficiently small size such that domain wall formation is energetically unfavorable, the demagnetization process can have several interesting features including quantum tunneling at sufficiently low temperatures.

The experimental conditions that drive a particular growth mechanism of CoPt (FePt) films and the linkage between crystallographic and morphological structure, vis-a-vis magnetocrystalline anisotropy, saturation and remanent magnetization, coercive field and magnetic domain structure need to be studied for each process of growth. Most of the earlier research on thin films of CoPt employed sputtering[1,2,3,4,5,6] or molecular beam epitaxy (MBE)[7,8] to grow textured and epitaxial films. The majority of these works have been carried out on (001) MgO substrates. The lattice parameter of MgO (cubic, a = 4.21 Å) is larger by 8.5 and 9.6 % compared to the basal plane unit cell parameter of $L1_0$ FePt and CoPt respectively. This large lattice mismatch invariably affects epitaxial growth and magnetic properties of the films, whose extent needs to be quantified by depositing fims on single crystal substrates which provide different degree of lattice mismatch.

One of the promising thin film growth techniques that has been used rarely for deposition of epitaxial CoPt is Pulsed Laser Deposition (PLD)[12]. One of the key advantages of PLD is a precise control over the stoichiometry of a multi-elemental film. This has been demonstrated amply in perovskite oxide films such as those of high T_c superconductors and hole-doped manganites. Additionally, the high adatom energy, which can be as large as $\simeq$ 400 eV in PLD can assist in stabilizing non-equilibrium phases[21]. Here we report PLD growth of epitaxial CoPt films on (001) cut $LaAlO_3$ (LAO), $SrTiO_3$ (STO) and MgO single crystals with the objectives to; (i) demonstrate the feasibility of growth of stoichiometric films from ablation of an alloy target, (ii) vary the extent of substrate induced strain by depositing films on single crystal substrates of different lattice parameter such that effects of both tensile as well compressive strain on growth morphology are addressed, (iii) establish correlations between film morphology, phase purity and magnetic properties, (iv) determine minimum growth temperature to stabilize the high coercive tetragonal phase, (v) address the role of kinetic conditions, such as deposition rate, in stabilizing a particular growth morphology at several growth temperatures and (vi), understand the demagnetization process in films of different microstructures.

We note that the surface morphology of these films depends strongly on deposition temperature (T_d) and growth rate (G_r), in addition to the lattice mismatch with the substrate, which can be characterized in terms of the strain parameter ϵ defined as $\epsilon = \frac{a_{bulk} - a_{substrate}}{a_{bulk}} \times 100$, where a is the lattice parameter. Values of the parameter ϵ for in-plane and out-of-plane c-axis growth of the $L1_0$ phase, and for the fcc phase on three different substrates used in this study are listed in Table - I. For MgO (001) [a = 4.21 Å], the ϵ for out-of-plane and in-plane c-axis growth of the $L1_0$ phase is - 10.7 % and - 13.8 % respectively. The films on STO (001) [a = 3.905 Å] also experience tensile strain in both orientations but it is nominal (ϵ = - 2.7 % for out-of-plane and - 5.5 % for in-plane c-axis growth) as compared to that on MgO (001). The (001) face of LAO [cubic, a = 3.792 Å], however provides an ideal square planar lattice with minimum lattice mismatch (- 2.5 and 0.3 % for in-plane and out-of-plane c-axis growth respectively) for epitaxial growth of the $L1_0$ phase of CoPt in either orientation. The choice of different ϵ allows tuning of the strain and hence the surface morphology of the films, provided the flux of adatoms on the substrate is kept low. At high flux densities, kinetic considerations eliminate the morphological features evolved due to an imbalance of strain and interfacial energies of the film. The best

c-axis oriented epitaxial $L1_0$ CoPt thin films display a coercive field ($H_{c\perp}$) as high as $\approx$ 30 kOe and anisotropy energy density of $\sim 4.62 \times 10^6$ J/m^3 at ambient temperature.

II. EXPERIMENTAL PROCEDURE

Cobalt-platinum films of equiatomic composition were grown by pulsed laser ablation of CoPt alloy target which was synthesized by arc melting of high purity (4N) cobalt and platinum chunks followed by homogenization at high temperature (900 ^{0}C). A KrF excimer laser (wavelength $\lambda = 248$ nm and pulse width $\sim$ 20 nsec) was used to ablate the 1 cm diameter target in an all-metal-seal PLD chamber maintained at 50 mTorr pressure of ultra high purity (99.9999 %) nitrogen. Three 3×3 mm^2 pieces, one each of MgO, STO and LAO, all (001) cut, were glued with silver epoxy on a substrate heater specially designed for ultra high vacuum applications. The buffer gas (N_2), which helps in reducing particulate density on the film surface, was pumped out on completion of growth to ensure that no stable nitrides of cobalt are formed when the film is cooled from the deposition temperature ($T_d \geq 600$ ^{0}C).

Three series of samples have been prepared under different growth conditions as listed in Table - II, to evaluate their effect on morphology, crystallographic structure and magnetic

properties of the films. The purpose of preparing each series is as follows; In series 'A' samples of $t_F \approx 100$ nm grown on (001) STO at 600, 700 and 800 ^{0}C the effects of T_d and post deposition annealing were studied. Series 'B' films were prepared to study the effect of film thickness. This series consists of four films of t_F ranging from 20 to 100 nm grown at 700 ^{0}C on STO and MgO substrates followed by annealing for 30 minutes at the growth temperature. The growth rate for these two sets of samples was ≈ 1 Å/sec. The last series, series 'C', was prepared at a slower growth rate (≈ 0.4 Å/sec). It consists of three set of samples deposited at 700, 750 and 800 ^{0}C on LAO, STO and MgO mounted side-by-side on the substrate heater. The thickness of these films was $\simeq 50$ nm. All thicknesses mentioned above were measured with a stylus based surface profilometer.

X-ray diffraction (XRD) measurements were performed using the Seifert model 3000P diffractometer with $CuK_{\alpha 1,\alpha 2}$ radiation in the standard θ - 2θ geometry with scattering vector normal to the plane of the film. The surface topography of the films was characterized using Scanning Electron Microscopy (SEM). The energy dispersive X-ray element analyzer of the same SEM was employed to ascertain the Co / Pt ratio in the ablation target as well as in films. Magnetic Force Microscopy (MFM) and Atomic Force Microscopy (AFM)

measurements were performed simultaneously on thermally demagnetized samples. A multi-mode AFM with a Nanoscope IV controller (Digital Instruments, Santa Barbara) was used in the tapping mode at a lift height of 50 nm to probe the magnetic domain structure in films. The MFM tip (CoCr coated Si) was magnetized vertically along the tip axis, thereby allowing detection of the perpendicular component of stray field emanating from the sample surface with a spatial resolution of $\approx$ 50 nm.

Measurements of magnetization and magnetic relaxation were carried out using a superconducting quantum interference device (SQUID) based magnetometer [Quantum Design MPMS 5XC]. Both in-plane and out-of-plane field orientations were used in these measurements and all data were corrected for the contribution of the substrate. The absolute value of moment has an error of $\pm$ 15 % due to the uncertainty in the measurement of sample volume. For the measurements of magnetic relaxation, sample was first magnetized at 300 K with a 46 kOe field applied along the easy axis, and then the moment was monitored as a function of time in a reversed field of strength varying from 0 to $\leq H_c$.

III. RESULTS AND DISCUSSION

A. Effects of growth temperature and post growth annealing:

In Fig. 1(a) we show the XRD profiles of the series 'A' samples (deposited on STO at 600, 700 and 800 ^{0}C) together with the diffraction profile of a bare substrate. The pattern for the sample deposited at 600 ^{0}C shows only one peak at $2\theta = 48.12^0$, which can be attributed to the (200) reflection of the disordered A1 (fcc) phase. This reflection developed into a doublet on increasing the T_d to 700 ^{0}C, and finally goes back to a single peak shifted to higher 2θ at T_d = 800 ^{0}C. The doublet seen here is due to the mixing of the (200) and (002) reflections of the $L1_0$ phase with some c-axis grains oriented parallel and others oriented perpendicular to the film plane. At the highest deposition temperature, i.e., 800 ^{0}C, although the (002) peak of the $L1_0$ phase becomes prominent, a discernible shoulder remains on its low angle side. A marked increase in the intensity and sharpness of (001), (002) and (003) peaks of this film indicates significant improvement in the degree of chemical ordering at the elevated T_d.

Fig. 1(b) presents the in-plane magnetization (M-$H_{\parallel}$) from + H_{max} to - H_{max} of the films whose X-ray diffraction data are shown in Fig. 1(a). Only half loops were taken to save

the SQUID time. Since there are three ordered variants of CoPt which may co-exist in the film, each with c-axis parallel to one of the cube edge directions i.e., [001], [010] and [100] of the substrate [see, inset Fig. 1(b)], the external field was applied parallel to the film plane at 45^0 with respect to the [100] and [010] direction of the substrate as shown in the lower inset of Fig. 1(b). The coercive field ($H_{c\|}$) deduced from these measurements is 104 Oe, 6 kOe and 8.4 kOe for the films deposited at 600, 700 and 800 ^{0}C respectively. Since the field for $H_{c\|}$ measurement was applied diagonally, the true value of $H_{c\|}$ would be the component of measured $H_{c\|}$ along the [100] or [010] direction. The correct $H_{c\|}$ deduced in this manner then become 74 Oe, 4.2 kOe and 5.9 kOe for the 600, 700 and 800 ^{0}C films respectively. Since all measurements of magnetization in parallel configuration were performed with field applied along [110], we will only refer to corrected value of $H_{c\|}$ unless otherwise specified.

The extremely low coercivity ($H_{c\|} \approx 74$ Oe) of the film deposited at 600 ^{0}C is consistent with our X-ray data which show only the disordered A1 phase at this T_d. Such a low coercivity has been reported by several workers[8,9,10,11] in their A1 phase CoPt films. For the film deposited at 700 ^{0}C, the $H_{c\|}$ increases to 4.2 kOe. This increase in $H_{c\|}$ is also consistent with X-ray diffraction results which show the formation of the $L1_0$ phase with grains of

c-axis in the plane of the substrate as well as perpendicular to it. Samples prepared at 800 ^{0}C display even higher $H_{c\|}$ ($\approx$ 5.9 kOe). Crystallographically, such films are mostly pure $L1_0$ phase with c-axis normal to the plane of the substrate.

There are three important features in the M-$H_{\|}$ data of Fig. 1(b) which need to be highlighted; (i) while the magnetization of the 600 ^{0}C film saturates at very low field ($\simeq$ 5 kOe), the film of T_d = 700 and 800 ^{0}C show a non-saturating tendency of magnetization even at the maximum applied field of $\approx$ 20 kOe, (ii) the total magnetic moment of the films goes down with the increasing deposition temperature, and (iii), the coercivity increases non-monotonically as the T_d increases from 600 to 800 ^{0}C. Since $L1_0$ CoPt system exhibits very high anisotropy field H_k ($\approx$ 123 kOe)[13] with c-axis as the easy-axis of magnetization, the volume fraction of the film whose c-axis lies perpendicular to the surface of the substrate would behave more like a paramagnet for an in-plane measuring field. This would lead to a non-saturating M-H curve. While the first two observations made on the magnetization data of Fig. 1(b) indicate that crystallographic domains of $L1_0$ phase with c-axis in the plane of the substrate exist in 700 and 800 ^{0}C films, their fraction decreases in 800 ^{0}C films as suggested by the low remanence and large coercivity of such films. The 600 ^{0}C film on

the other hand is single-phase disordered fcc with its characteristically small H_c.

We have also studied the effects of thermal annealing on crystal structure and magnetization of a film deposited at 700 ^{0}C on STO. A 30 minutes anneal causes a significant enhancement in the degree of chemical ordering with c-axis of the ordered phase aligned parallel to the film normal. The observed increase in coercivity from 4.2 kOe to 5.9 kOe on annealing is consistent with the results of structural analysis.

B. Effect of film thickness (t_F) and epitaxial strain:

Fig. 2(a) shows a series of XRD patterns for films (series B) of thickness ranging from 30 to 100 nm grown on STO at 700 ^{0}C and annealed at the same temperature for 30 minutes. The fundamental and superlattice peaks of the $L1_0$ phase are observed clearly in all the samples. We also note that with the increasing thickness, the intensity of the (200) reflection of $L1_0$ increases and for 100 nm thick film it becomes equal to the intensity of the (002) peak. The M-H curves for in-plane magnetization $M(H_\parallel)$ and the morphology of these films are shown in Fig. 2(b) and Fig. 2(c, d, e) respectively. We observe an interconnected maze-like pattern of CoPt layer in the 20 nm thick film. On increasing the thickness to 30 nm, the void fraction in the film decreases, and at t_F = 50 nm, the percolating network

expands at the expense of the voids and the film becomes almost continuous.

A set of samples was also prepared on MgO substrates, loaded side-by-side to STO whose results have been discussed in the preceding section. The XRD profiles, M-$H_{\parallel}$ curves and surface morphology of these samples are presented in Fig. 3. Interestingly, the morphological features of these films are similar to those deposited on STO [Fig. 2] in spite of a large difference in strain parameters ϵ_{MgO} and ϵ_{STO}. It appears that the higher G_r ($\approx$ 1 Å/sec) used here and the moderate growth temperature ($\sim$ 700 ^{0}C), conspire to increase the supersaturation of adatoms on the surface of the substrate which reduces the critical size of a cluster beyond which it does not grow, and increase the cluster nucleation rate[22,23]. These two factors appear to suppress the effect of strain leading to a similar morphology of the films deposited on STO and MgO.

Fig. 3(a) shows the XRD profiles of the 30, 50 and 100 nm thick films grown on MgO. These results reveal that unlike the films on STO, MgO favors a growth with c-axis of the $L1_0$ phase in the plane of the substrate. Here the intensity of the (200) peak (I_{200}) increases faster than that of the (002) peak (I_{002}). In the inset of Fig. 4 we plot the variation of I_{200}/I_{002} for the films deposited on MgO and STO as a function of their thickness. It is

expected that the increased fraction of the c-axis in-plane phase on MgO with increasing t_F should lead to a distinct increase in the low-field magnetization for in-plane measurements. Our data for $M(H_{\parallel})$ (Fig. 4(b)) however, do not reveal a clear trend with t_F within the accuracy ($\pm$ 15 %) of these measurements. The in-plane coercivity ($H_{c\parallel}$) of these films as a function of their thickness is plotted in Fig. 4. A marginal enhancement in coercivity is seen as the films are made thinner. By comparing this result with the microstructure of the films, it becomes clear that a percolative network is more coercive than a continuous film.

In order to understand the magnetization reversal process in films of ordered $L1_0$ phase with mixed crystallographic domains, some with their c-axis parallel and other perpendicular to the substrate plane, we have measured the magnetization of the series 'B' samples [T_d = 700 ^{0}C] grown on STO in $H_{\parallel}$ and $H_{\perp}$ geometries. The magnetic field for the in-plane ($H_{\parallel}$) measurements was applied at 45^0 with respect to the [100] and [010] direction of the substrate as mentioned in the previous section. The component of $H_{c\parallel}$ along [100] or [010] direction is expected to be equal to $H_{c\perp}$ if the three variants of c-axis are present with equal abundance. Interestingly, the calculated values of the $H_{c\parallel}$ along [100] and [010] (listed in Table -II) match reasonably well with the measured values of $H_{c\perp}$ irrespective of the film

thickness.

C. Fractals and nano-dots at low growth rate:

The evolution of film morphology with deposition temperature and growth rate is intimately linked with the epitaxial strain parameter ϵ, provided the growth rate is not large[6,12]. In order to study the strain induced crystallographic and morphological changes, a set of samples (series 'C') was prepared using a slow deposition rate ($\approx$ 0.4 Å/sec) on (001) LAO, (001) STO and (001) MgO. From the XRD data we could not conclude whether there exist any c-axis variants in the film on LAO when grown at 700 ^{0}C because the position of the (200) reflection in θ - 2θ scan is same as of the (002) (using pseudocubic unit cell) reflection of the substrate. But there is a clear signature of this in films deposited on the other two substrates. It was also evident from the relative intensity of the (200) and (002) reflections that the fraction of the domains with in-plane c-axis is more in the film on MgO as compared to that in the film on STO. The c-axis lattice parameter of these films calculated from the position of the (002) reflection shows a small but distinct drop at the higher growth temperatures (see Fig. 5). This change is independent of the substrate used. At the highest deposition temperature i.e., 800 ^{0}C, the c-axis lattice parameter for films on all the three

substrates compare reasonably well with the bulk value of 3.701 Å.

The SEM micrographs of the surface of these films present some interesting manifestations of epitaxial strain. As seen in Fig. 6(a) for the film deposited on STO at 700 ^{0}C, the morphology is a self-similar fractal where the fractals do not form a percolating backbone over a length scale larger than $\simeq$ 5 μm. On increasing the T_d to 750 ^{0}C, the maze-like structure breaks up into islands. A similar morphology is seen in films deposited on MgO at 750 ^{0}C. Upon further increase of T_d to 800 ^{0}C, the islands on STO acquire a smaller and nearly uniform size distribution ($\simeq$ 200 nm) [Fig. 6(c)]. The values of the thermal expansion coefficients of STO and MgO (11.1 $\times$ 10^{-6} K^{-1} and 12.8 $\times$ 10^{-6} K^{-1}, respectively[24]) are close to that of CoPt (10.9 $\times$ 10^{-6} K^{-1}[25]). These data suggest that the ϵ parameter at T_d does not differ much from its room temperature value for MgO as well as STO. The breaking of the films can, therefore, be understood on the basis of the strain parameter calculated using room temperature lattice constants. The reason for these changes in film morphology can be argued to depend on the imbalance of interfacial and strain energies that minimizes the contact area between film and the substrate with increasing T_d[6].

The most interesting case is when the films are grown on LAO which has nearly perfect

lattice match (ϵ = + 0.3 %) with the out-of-plane $L1_0$ CoPt at room temperature. As evident from Fig. 7 there is an irregular shaped island growth on LAO even at 700 ^{0}C. Since the coefficient of thermal expansion for LAO (9.2×10^{-6} K^{-1}) is similar to that of CoPt[24], this breaking of the film can not be explained on the basis of strain alone. However, LAO undergoes a structural phase change from rhombohedral to cubic symmetry on heating above 800 ^{0}K[26]. The lattice parameter and associated expansion coefficient of the cubic phase perhaps facilitate the island growth seen at 700 ^{0}C. The island morphology becomes sharper on increasing the T_d to 800 ^{0}C. This nanoscale structure that evolves at the higher T_d and low G_r is likely to be due to the enhanced desorption of adatoms from surface which leave large areas with little or no coverage. These regions can host new islands[27]. Similar observations have been made by Castaldi et al[16] for CoPt films deposited on oxidized Si substrates using electron beam evaporation technique.

D. Magnetic behavior of the fractals and nano-dots grown on STO:

We have addressed the magnetization and demagnetization characteristics of the films deposited at low growth rate ($G_r \approx 0.4$ Å/sec) on STO (series C) in detail. The typical M-H loops at 300 K of the samples grown at 700, 750 and 800 ^{0}C are shown in Fig. 6 (d,

e and f) respectively. These data are for field applied perpendicular to the plane of the film ($H_{\perp}$), except for 800 ^{0}C sample for which $H_{\parallel}$ measurement is also shown. A striking feature of these data is a substantial increase in coercivity ($H_{c\perp}$) [see Table - II] with the increasing deposition temperatures. In order to understand the magnetization dynamics and its reversal mechanism let us consider the three samples separately.

Sample deposited at 700 ^{0}C does not show any saturation of the magnetic moment even at 30 kOe. The coercive field $H_{c\perp}$ in this case is $\approx$ 7 kOe. We have already discussed the presence of c-axis variants of $L1_0$ phase with grains of c-axis parallel to [100] and [010] directions of the substrate for the sample deposited at 700 ^{0}C. Since c-axis is the easy-axis of magnetization in $L1_0$ phase of CoPt film, the fraction of $L1_0$ phase with in-plane c-axis play a major role in setting the magnetic response of the sample. The paramagnet-like contribution to magnetization of the in-plane c-axis fraction of CoPt when the field is applied perpendicular to substrate surface would display a non-saturating tendency of magnetic moment even at very high fields because of the large uniaxial anisotropy ($H_k \approx$ 123 kOe) of $L1_0$ CoPt phase. The remanence squareness S (= M_r/M_s), where M_s and M_r are the saturation and remanent magnetization respectively, of the series 'C' samples is plotted

in Fig. 8 as a function of T_d. The S parameter is $\simeq 0.85$ for the 700 ^{0}C deposited films. Although a high value of S (> 0.5) has been attributed to exchange coupling amongst the particles[15], we believe that the large S seen in this sample of a fractal-like morphology is a manifestation of pinning of the domain walls by the boundaries between adjacent c-axis variants where the easy axis changes by 90 ^{011}.

For the sample deposited at 800 ^{0}C the saturation field is beyond the maximum dc-field (46 kOe) used in these M ($H_\perp$) measurements. This is indicated by the hysteresis loop shown in Fig. 6(f), which is neither symmetrical nor centered about the origin, and has no reversible region even at the maximum applied field. A very large $H_{c\perp}$ of ≈ 30 kOe is seen in these films. It is important to mention here that this $H_{c\perp}$ has been derived by taking the average of the magnetic field corresponding to zero moment from both sides of the hysteresis loop. The true $H_{c\perp}$ may be still higher because the loop did not reach saturation due to the limited value of the applied field[28]. Fig. 6(f) also shows the M-H curve taken in the parallel field configuration. The uniaxial magnetic anisotropy K_u of this film, determined from the area enclosed by the parallel and perpendicular magnetization curves, comes out to be $\approx 4.62 \times 10^6$ J/m^3, which is very close to the maximum value ($\sim 5.0 \times 10^6$ J/m^3) reported in

the literature[29].

In order to establish a correlation between morphological features and magnetic domain structure of the films of the series 'C', we show in Fig. 9 the atomic and magnetic force micrographs (AFM and MFM respectively) taken from the same spot on the film. For the 750 ^{0}C sample, there is some discrepancy between the SEM image (Fig. 6(b)) and the AFM image (Fig. 9(a)). While the SEM image shows well-separated grains, the AFM image reveals a much smaller separation between them. The MFM image of this sample suggests that the magnetic domains are not confined to a physical grain, and also the boundary between two adjacent domains is not sharp. This clear non-conformity of the topographical structure and magnetic domain pattern suggest that the grain boundaries do not play a significant role in pinning of domains and their reversal. The AFM image of the sample grown at 800 ^{0}C (Fig. 9(b)) is quite similar to its SEM image (Fig. 6(c)) which shows uniform and well-separated nano grains. The MFM image of individual grains does not show any domain boundaries. Since one can exactly map each feature of the AFM image onto the MFM image, it is clear that each grain in the film is a single magnetic domain. The bright and dark features in the MFM image, which represent nano grains of reversed

magnetization are similar in number, ensuring zero magnetization in the thermally demagnetized state. Another interesting aspect of this image is that the bright and dark features tend to group among themselves showing string-like structures and islands. Although the remanence squareness parameter S ($\simeq 0.59$) for this sample is close to that for a randomly oriented assembly of non-interacting Stoner-Wohlfarth (S-W) particles[15,19], we cannot really rule out interaction between the particles. Further, a limited spatial resolution of MFM ($\approx$ 50 nm) also makes it difficult to say whether the demagnetization process is via a coherent rotation of magnetization or due to a curling mode which can lead to vorticity in the spin system.

E. Relaxation of magnetization in single-domain nano-dots:

In order to understand the process of magnetization reversal, relaxation measurements of magnetization at constant negative bias field close to the coercive value ($H_{c\perp}$) were carried out on film deposited at 800 ^{0}C (series 'C'). The theory of thermal fluctuation of the magnetic moment of single-domain ferromagnetic particles was introduced by Néel[30] and further developed by Brown[31]. For the particles at zero applied field, the energy barrier between two equilibrium states of opposite moment is too high to observe magnetization reversal in a

reasonable experimental time scale of a few hours. However, by applying a reverse field close to the coercive field H_c after fully magnetizing the particle, reversal can be initiated through thermal activation process within a short time scale. In our relaxation measurements, the sample was first magnetized at 300 K in a field of 46 kOe applied perpendicular to its plane. The field was then reversed to a desired value H ($\leq H_{c\perp}$) in one step, and sample moment was monitored as a function of time over a period of 2.5 hours. Fig. 10 shows the decay of magnetization as a function of time at different values of reversed field. The presence of two distinct regimes of time in the figure indicates that there are two different activation processes leading to the relaxation of the system. A distribution in grain size is a possible reason for this behavior. The data of Fig. 10 have been fitted to the Néel-Brown model[32] for relaxation given as $M(t) = M_0 \exp(-t/\tau)$, where M_0 is the magnetization at t = 0 and M(t) the remanent magnetization at time t after removal of the field, τ is the relaxation time defined as $1/\tau = f_0 \exp(-E(H)/k_\beta T)$, f_0 is a frequency factor of the order of 10^9 sec^{-1} and $E(H) = K_u V(1 - H/H_k)^2$ the energy barrier in a reverse field of magnitude H. Here V, K_u and H_k denote particle volume, anisotropy energy density and anisotropy field ($=2K_u/M_s$) respectively[33]. It appears that the relaxation rate of magnetization increases rapidly as the

absolute value of the magnetic field is increased. Using the above formula and approximating the grains to be of a spherical shape, we extract the activation volume whose width is $\approx$ 4.7 nm. This is far less than the diameter ($\approx$ 200 nm) of the disc-shaped magnetic particles seen in SEM and MFM micrographs. This discrepancy points towards inadequacy of the model used.

The relaxation behavior of an assembly of single-domain particles can deviate from the ideal Néel - Brown picture due to several reasons which include, multi-domain nature of particles, interaction between the particles and a distribution in their size. Our MFM images, however, do not show any well-defined sub-domains in the nano grains. Interaction amongst particles, on the other hand, leads to an apparent enhancement rather than a decrease in the activation volume. One could argue that the demagnetization process occurs via a curling mode in which the magnetization continuously curls around the particle center[34]. This can, in principle, lead to a smaller activation energy for demagnetization. A simple calculation for our disc-shaped grains of diameter $\approx$ 200 nm and thickness $\approx$ 50 nm with anisotropy axis perpendicular to the disc plane shows that reversed spins on a circular ring of width $\approx$ 60 nm around the periphery of the disc would be sufficient to make the net magnetization

zero. However, the presence of such a curing mode can not be established with MFM due to its limited resolution. Further work, preferably with spin polarized tunneling, as done in the case of Fe platelets grown on (110) surface of tungsten[35] may shed more light on the demagnetization dynamics of these CoPt nano-dots.

IV. CONCLUSIONS

CoPt films of 20 to 100 nm thickness were successfully grown using the Pulsed Laser Deposition (PLD) technique by ablating a $Co_{50}Pt_{50}$ alloy target. The deposition conditions which facilitate growth of the $L1_0$ ordered phase of high magnetocrystalline anisotropy are clearly identified. Correlations between film morphology, crystallographic structure and magnetic properties such as magnetocrystalline anisotropy, shape and size of the hysteresis loops, coercive field and magnetic domain structure etc. have been established. We note that the crystallographic ordering in films deposited at 600 ^{0}C on single crystal substrates which offer different degree of strain is similar. These films have a disordered fcc structure with in-plane magnetization and a narrow hysteresis loop of width $\approx$ 200 Oe. The near-complete chemical ordering achieved at $T_d \geq 700$ ^{0}C, becomes predominantly c-axis oriented as the deposition temperature is raised to 800 ^{0}C. While the changes in the crystallographic

structure of the films depend solely on T_d, their microstructure and magnetization characteristics are decided by the growth rate. It is observed that irrespective of a large difference in lattice parameters of the substrates used, there is hardly any change in morphology of the films grown on different substrates, when a high growth rate ($\approx$ 1 Å/sec) is maintained. The microstructure of these $L1_0$ films evolves from a well-connected maze-like structure at t_F = 20 nm to a smooth and continuous film at t_F = 50 nm. The magnetic coercivity of these films increases as the $L1_0$ phase fraction grows with T_d and its orientation becomes out of the film plane.

While the higher growth rate seems to suppress the effects of strain due to lattice mismatch, low growth rate ($\approx$ 0.4 Å/sec) reveals granularity in the films even at small thickness ($\approx$ 50 nm). Here the structure changes from a self-similar fractal pattern to nano-dots as the T_d is raised from 700 to 800 ^{0}C. The reason for this topographical change appears to be the imbalance between strain and interfacial energies, which is overridden by kinetic considerations at the high growth rates. The AFM and MFM images of the films grown at low G_r and high T_d reveal physically separated, magnetically single-domain nano-scale islands. Magnetic relaxation measurements carried out to study the relaxation dynamics

of these single-domain islands show negligible decay of magnetization unless a reverse field close to the coercive field ($H_c \approx 30$ kOe) is applied. The simple picture of coherent rotation of magnetization appears incompatible with the time dependence of the remanent magnetization.

This research has been supported by a grant from the National Nanoscience & Nanotechnology Initiative of the Department of Science & Technology, India.

REFERENCES:

[1] T. Shima, K. Takanashi, Y. K. Takanashi, and K. Hono, Appl. Phys. Lett. **85**, 2571 (2004).

[2] S. H. Liou, Y. Liu, S. S. Malhotra, M. Yu, and D. J. Sellmyer, J. Appl. Phys. **79**, 5060 (1996).

[3] S. Jeong, M. E. McHenry, and D. E. Laughlin, IEEE Trans. Magn. **37**, 1309 (2001).

[4] P. D. Kim, I. A. Turpanov, S. V. Stolyar, R. S. Lskhakov, V. I. Yushkov, A. Y. Beten'kova, L. A. Li, E. V. Bondareva, T. N. Isaeva, and M. M. Karpenko, Solid-State Electron. **49**, 431 (2004).

[5] K. Barmak, J. Kim, R. A. Ristau, and L. H. Lewis, IEEE Trans. Magn. **34**, 2799 (2002).

[6] M-G Kim and S-C Shin, J. Appl. Phys. **90**, 2211 (2001).

[7] R. F. C. Farrow, D. Weller, R. F. Marks, M. F. Toney, A. Cebollada, and G. R. Harp, J. Appl. Phys. **79**, 5967 (1996).

[8] O. Ersen, V. Parasote, V. Pierron-Bohnes, M. C. Cadeville, and C. Ulhaq-Bouillet, J. Appl. Phys. **93**, 2987 (2003).

[9] S-E Park, P-Y Jung, and K-B Kim, J. Appl. Phys. **77**, 2641 (1995).

[10] Q. F. Xiao, E. Brück, Z. D. Zhang, F. R. Boer, and K. H. J. Buschow, J. Appl. Phys. **91**, 8819 (2002).

[11] R. A. Ristau, K. Barmak, L. H. Lewis, K. R. Coffey, and J. K. Howard, J. Appl. Phys. **86**, 4527 (1999).

[12] R. K. Rakshit, S. K. Bose, R. Sharma, and R. C. Budhani, Appl. Phys. Lett. **89**, 202511 (2006).

[13] D. Weller, A. Moser, L. Folks, M. E. Best, W. Lee, M. F. Toney, M. Schwickert, J-U Thiele, and M. F. Doerner, IEEE Trans. Magn. **36**, 10 (2000).

[14] T. Aoyama, K. Uchiyama, T. Kagotani, K. Hattori, Y. Wada, S. Okawa, H. Hatate, H. Nishio, and I. Sato, IEEE Trans. Magn. **37**, 1646 (2001).

[15] H. Zeng, J. Li, Z. L. Wang, J. P. Liu, and S. Sun, IEEE Trans. Magn. **38**, 2598 (2002).

[16] L. Castaldi, K. Giannakopoulos, A. Travlos, and D. Niarchos, Appl. Phys. Lett. **85**, 2854 (2004).

[17] R. K. Rakshit and R. C. Budhani, J. Phys. D: Appl. Phys. **39**, 1743 (2006).

[18] J. B. Newkirk, R. Smoluchowski, A. H. Geisler, and D. L. Martin, J. Appl. Phys. **22**, 290 (1950).

[19] E. C. Stoner, F. R. S., and E. P. Wohlfarth, IEEE Trans. Magn. **27**, 3475 (1991).

[20] J. D. Livingston, J. Appl. Phys. **52**, 2544 (1981).

[21] J. C. S. Kools in *Pulsed Laser Deposition of Thin Films*, edited by D. B. Chrisey and G. K.

Hubler (John Wiley & Sons Inc., New York, 1994), chap. 19, p. 455.

[22] J. S. Horwitz and J. A Sprague in *Pulsed Laser Deposition of Thin Films*, edited by D. B. Chrisey and G. K. Hubler (John Wiley & Sons Inc., New York, 1994), chap. 8, p. 229.

[23] J. E. Greene in *Multicomponent and Multilayered Thin Films for Advanced Microtechnologies*, edited by O. Auciello and J. Engemann (Kluwer Academic Publishers, Netherlands, 1993), NATO/ASI series **E234**, p. 39.

[24] K - S Hwang, B - A Kang, Y - S Jeon, J - H An, B - H Kim, K. Nishio, and T. Tsuchiya, Surf. Coat. Technol. **190**, 331 (2005).

[25] W. M. Liao, S.K. Chen, F.T. Yuan, C.W. Hsu, and H.Y. Lee, J. Magn. Magn. Mater. **303**, e243 (2006).

[26] Q. Zhang and P. J. McGinn, J. Eur. Ceram. Soc **25**, 407 (2005).

[27] P. Jensen, H. Larralde, M. Meunier, and A. Pimpinelli, Surf. Sci. **412-413**, 458 (1998).

[28] I. S. Jacobs and C. P. Bean in *Magnetism*, edited by G. T. Rado and H. Suhl (Academic Press Inc., London, 1963), Vol. III, chap. 6, p. 271.

[29] R. A. McCurrie and P. Gaunt, Philos. Mag. **13**, 567 (1966).

[30] J. Néel, Ann. Geophys. **5**, 99 (1949).

[31] W. F. Brown, Phys. Rev. **130**, 1677 (1963).

[32] E. P. Wohlfarth, J. Phys. F: Met. Phys. **14**, L155 (1984).

[33] R. W. Chantrell and K. O'Grady in *Magnetic Properties of Fine Particles*, edited by J. L. Dormann and D. Fiorani (Elsevier Science Publishers B. V., Netherlands, 1992), chap. 3, p. 103.

[34] H. Zijlstra in *Ferromagnetic Materials*, edited by E. P. Wohlfarth (North-Holland Publishing Company, New York, 1982), vol. 3, p. 37.

[35] A. Wachowiak, J. Wiebe, M. Bode, O. Pietzsch, M. Morgenstern, and R. Wiesendanger, Science **298**, 577 (2002).

TABLE I: Strain parameter ϵ for the growth of fcc and $L1_0$ CoPt on different substrates. The lattice parameter of LAO, MgO and STO substrates are 3.792 Å, 4.21 Å and 3.905 Å respectively. While CoPt in fcc phase is cubic with lattice parameter of 3.772 Å, the lattice parameters of the $L1_0$ CoPt in the bulk form are a = b = 3.803 Å and c = 3.701 Å.

substrate	crystallographic structure of CoPt	growth direction	ϵ
LAO (001)	fcc	–	- 0.5 %
LAO (001)	$L1_0$	in-plane c-axis	- 2.5 %
LAO (001)	$L1_0$	out-of-plane c-axis	+ 0.3 %
MgO (001)	fcc	–	- 11.6 %
MgO (001)	$L1_0$	in-plane c-axis	- 13.8 %
MgO (001)	$L1_0$	out-of-plane c-axis	- 10.7 %
STO (001)	fcc	–	- 3.5 %
STO (001)	$L1_0$	in-plane c-axis	- 5.5 %
STO (001)	$L1_0$	out-of-plane c-axis	- 2.7 %

TABLE II: Sample preparation conditions for different series of films. The table also lists the in-plane and out-of-plane coercive field of the films.

series	G_r	t_F	T_d	substrate	post growth annealing	$H_{c\parallel}/H_{c\perp}$
	($\approx$ Å/sec)	(nm)	(^{0}C)		time (minutes)	(kOe)
A	1	100	600	STO	No	0.074/–
	1	100	700	STO	No	4.2/–
	1	100	800	STO	No	6/–
	1	100	700	STO	30	5.9/–
B	1	20	700	STO	30	–/–
	1	30	700	STO	30	6.4/6.7
	1	50	700	STO	30	6.2/5.1
	1	100	700	STO	30	5.4/4.3
	1	20	700	MgO	30	–/–
	1	30	700	MgO	30	8.3/–
	1	50	700	MgO	30	7.9/–
	1	100	700	MgO	30	6.8/–
C	0.4	50	700	LAO	25	–/–
	0.4	50	750	LAO	25	–/–
	0.4	50	800	LAO	25	–/–
	0.4	50	700	MgO	25	–/–
	0.4	50	750	MgO	25	–/–
	0.4	50	800	MgO	25	–/–
	0.4	50	700	STO	25	–/7
	0.4	50	750	STO	25	–/16
	0.4	50	800	STO	25	0.4/37

FIGURE CAPTIONS:

FIG. 1. (a) X-ray diffraction profiles of the 100 nm films deposited at various temperatures on (001) cut STO. The diffraction profile of a bare substrate is also shown (bottom panel). Arrows in the top panel mark the position of fundamental as well as superlattice reflections of the $L1_0$ ordered phase. (b) In-plane magnetization of the same set of samples whose XRD is shown in Fig. 1(a). A sketch of the direction of in-plane field $H_{\parallel}$ is shown in the lower inset of the figure. The upper inset represents a schematic of the three c-axis variants of the $L1_0$ phase.

FIG. 2. (a) X-ray diffraction profiles of CoPt thin films of various thickness deposited at 700 ^{0}C on STO (001) at a growth rate of $\approx$ 1 Å/sec. All the samples were annealed for 30 minutes at the growth temperature. The diffraction profile of single crystal STO (001) is also shown (bottom panel). Arrows in Fig. 2(a) indicate the position of fundamental as well as superlattice reflections of the $L1_0$ phase. Dotted line in the figure marks the position of the (200) reflection. In-plane magnetization curves of the same set of samples are shown in panel (b). Panels (c), (d) and (e) show SEM micrographs of the samples of different thickness.

FIG. 3. (a) X-ray diffraction profiles of CoPt thin films of various thickness deposited at 700 ^{0}C on MgO (001) at a growth rate of $\approx$ 1 Å/sec. All the samples were annealed for 30 minutes at the growth temperature. The diffraction profile of single crystal MgO (001) is also shown (bottom panel). Arrows in the figure indicate the position of fundamental as well as superlattice reflections of the $L1_0$ phase. Dotted line in the figure marks the position of the (200) reflection. Panel (b) shows the in-plane magnetization of the same set of samples. Panels (c), (d) and (e) show SEM micrographs of the samples of different thickness.

FIG. 4. Variation of the in-plane coercive field $H_{c\|}$ with thickness for the films on STO and MgO deposited at 700 ^{0}C at a growth rate of $\approx$ 1 Å/sec. Inset shows the dependence of I_{200}/I_{002} on film thickness. All the samples were annealed for 30 minutes at the growth temperature. Solid lines in the figure are guide to the eye.

FIG. 5. The c-axis lattice parameter plotted as a function of the deposition temperature of the films on LAO, STO and MgO at a rate of $\approx$ 0.4 Å/sec. All the samples were annealed for 25 minutes at growth temperature.

FIG. 6. SEM images and perpendicular magnetization loops of 50 nm CoPt thin films deposited at various substrate temperatures at a growth rate of $\approx$ 0.4 Å/sec on single

crystal STO (001). All the samples were annealed for 25 minutes. Magnetization panel (f) for the sample grown 800 ^{0}C also shows data for in-plane configuration of the magnetic field.

FIG. 7. SEM images of of 50 nm CoPt thin films deposited at 700 and 800 ^{0}C with a growth rate of $\approx$ 0.4 Å/sec on single crystal LAO (001). These samples were annealed for 25 minutes at the growth temperature.

FIG. 8. Variation of remanent ratio S and perpendicular coercive field $H_{c\perp}$ with deposition temperature for 50 nm CoPt thin films deposited at a growth rate of $\approx$ 0.4 Å/sec on single crystal STO (001). All the samples were annealed for 25 minutes at the growth temperature.

FIG. 9. (color online). AFM and MFM images of 50 nm CoPt thin films deposited at (a) 750 ^{0}C and (b) 800 ^{0}C at a growth rate of $\approx$ 0.4 Å/sec on STO (001). Measurements were carried out on thermally demagnetized samples.

FIG. 10. Magnetic relaxation data collected at T =300 K for different values of the bias field. The sample was initially magnetized at 46 kOe. Solid lines are fit to the Néel-Brown equation for relaxation[32].

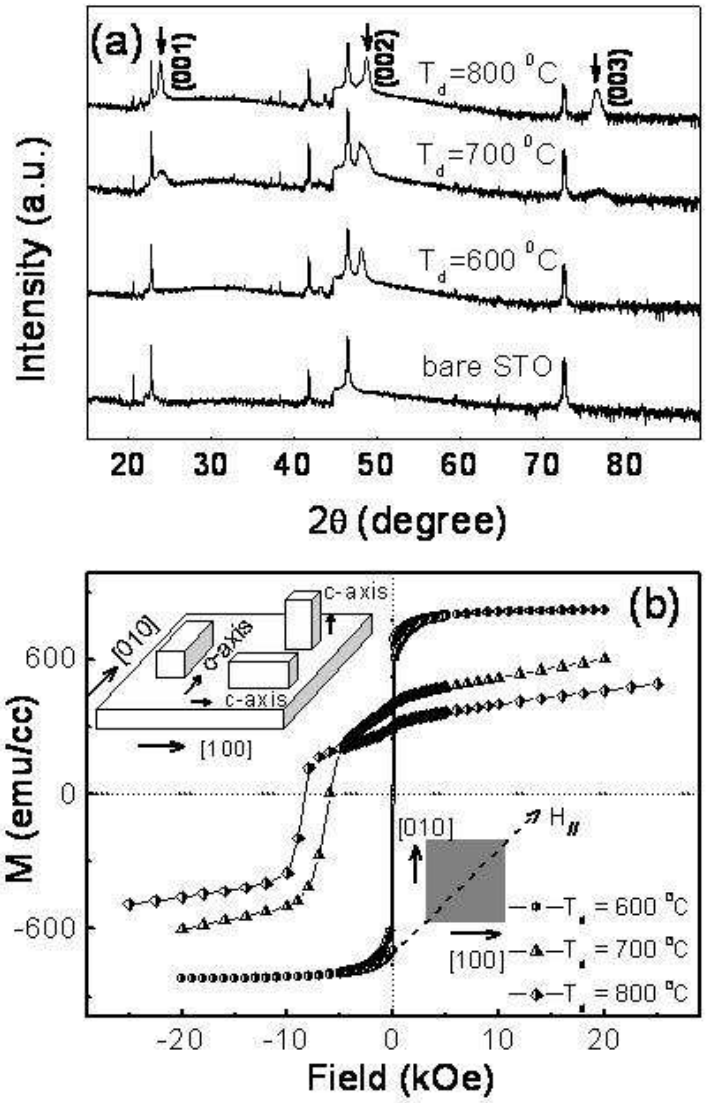
(a)
(001)
(002)
(003)
T_d=800 °C
T_d=700 °C
T_d=600 °C
bare STO
Intensity (a.u.)
20
30
40
50
60
70
80
2θ (degree)
(b)
c-axis
[010]
c-axis
c-axis
[100]
600
0
-600
M (emu/cc)
[010]
H//
[100]
T_d = 600 °C
T_d = 700 °C
T_d = 800 °C
-20
-10
0
10
20
Field (kOe)

FIG: 1

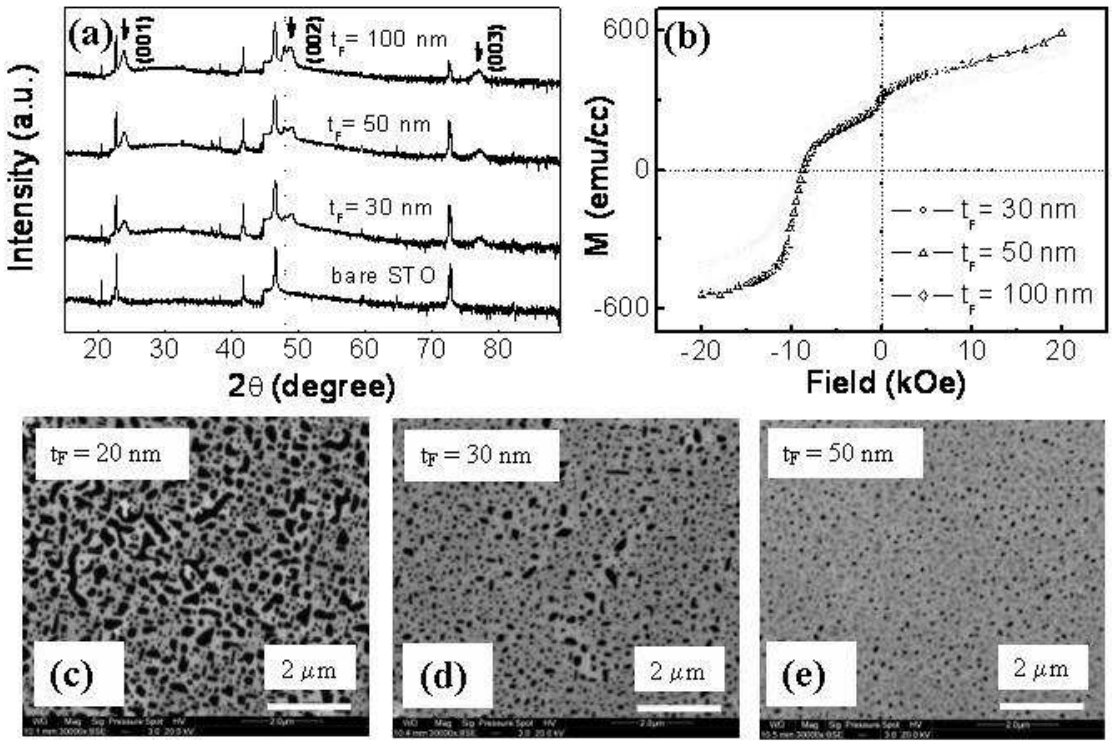
(a)
(001)
(002)
(003)
t_F = 100 nm
t_F = 50 nm
t_F = 30 nm
bare STO
Intensity (a.u.)
20 30 40 50 60 70 80
2θ (degree)
(b)
600
0
-600
M (emu/cc)
t_F = 30 nm
t_F = 50 nm
t_F = 100 nm
-20 -10 0 10 20
Field (kOe)
t_F = 20 nm
(c)
2 μm
t_F = 30 nm
(d)
2 μm
t_F = 50 nm
(e)
2 μm

FIG: 2

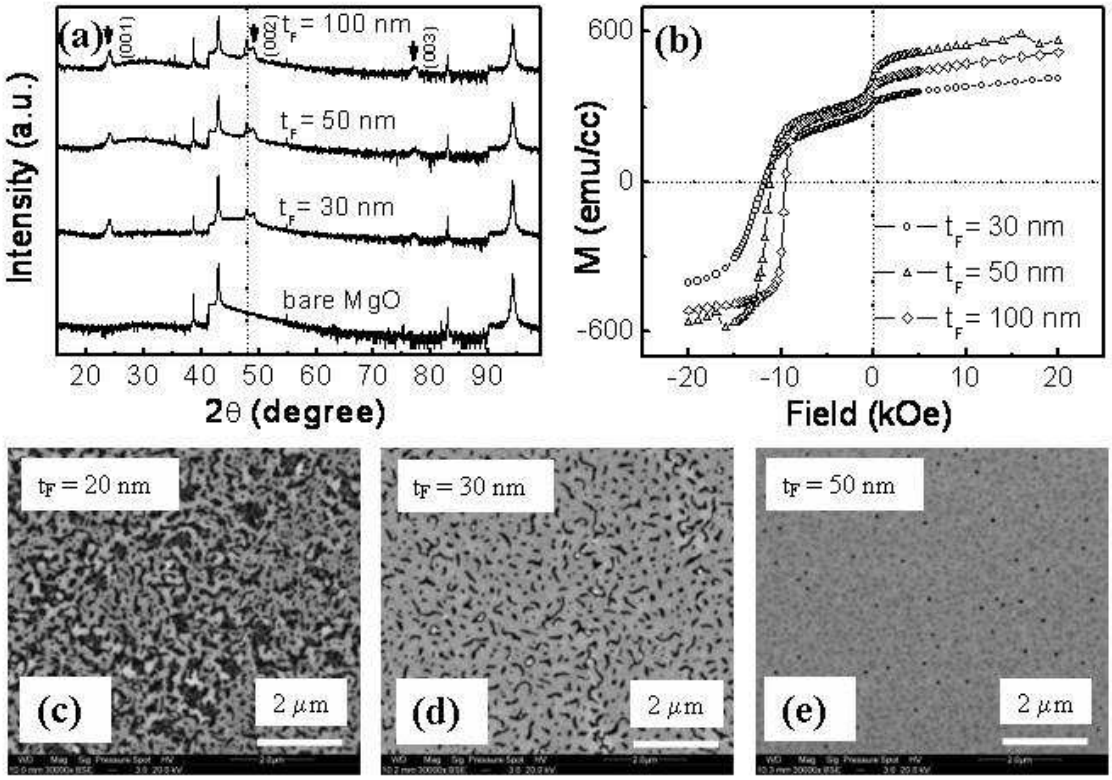
(a)
(001)
(002)
(003)
t_F = 100 nm
t_F = 50 nm
t_F = 30 nm
bare MgO
Intensity (a.u.)
20 30 40 50 60 70 80 90
2θ (degree)
(b)
600
0
-600
M (emu/cc)
t_F = 30 nm
t_F = 50 nm
t_F = 100 nm
-20 -10 0 10 20
Field (kOe)
t_F = 20 nm
(c)
2 μm
t_F = 30 nm
(d)
2 μm
t_F = 50 nm
(e)
2 μm

FIG: 3

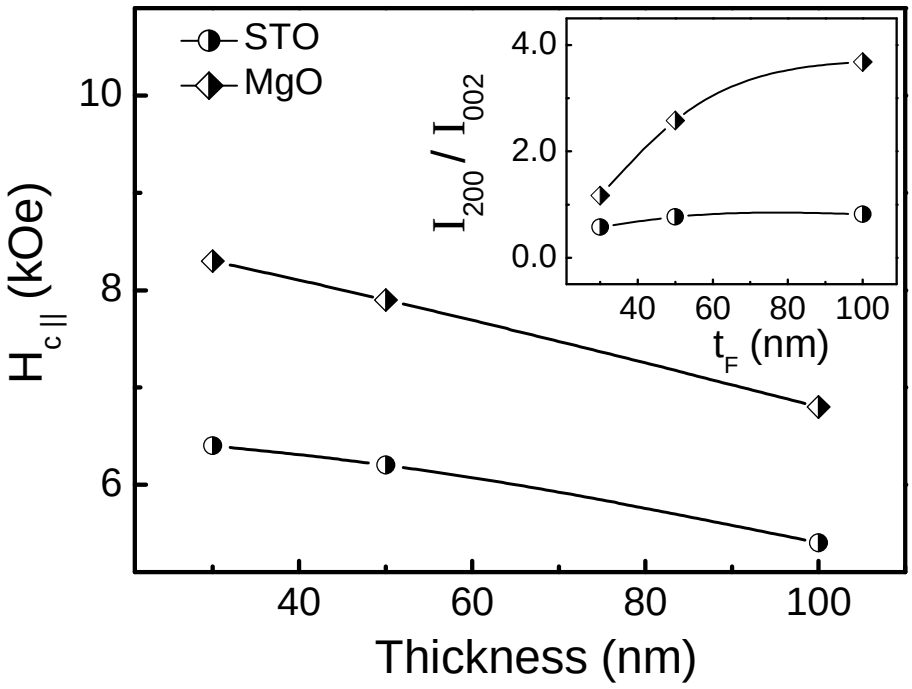
STO
MgO
10
8
6
$H_{c\perp}$ (kOe)
40
60
80
100
Thickness (nm)
I_{200} / I_{002}
4.0
2.0
0.0
40
60
80
100
t_F (nm)

FIG: 4

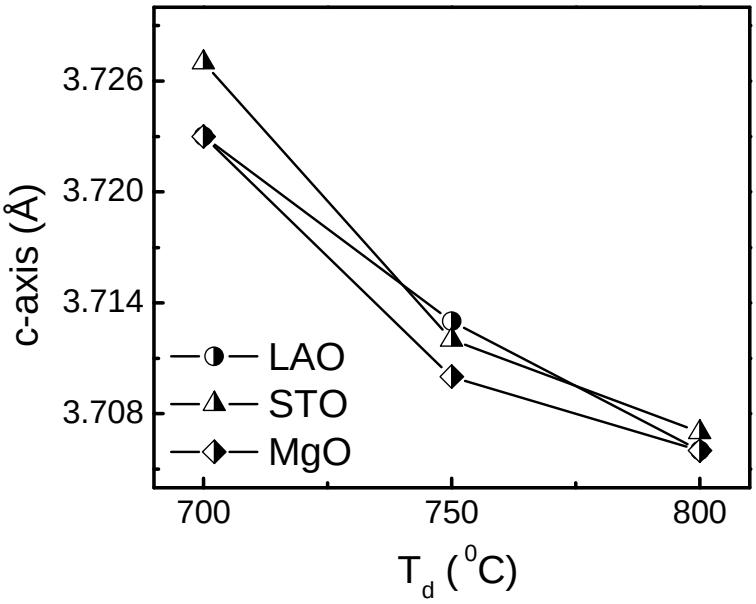

FIG: 5

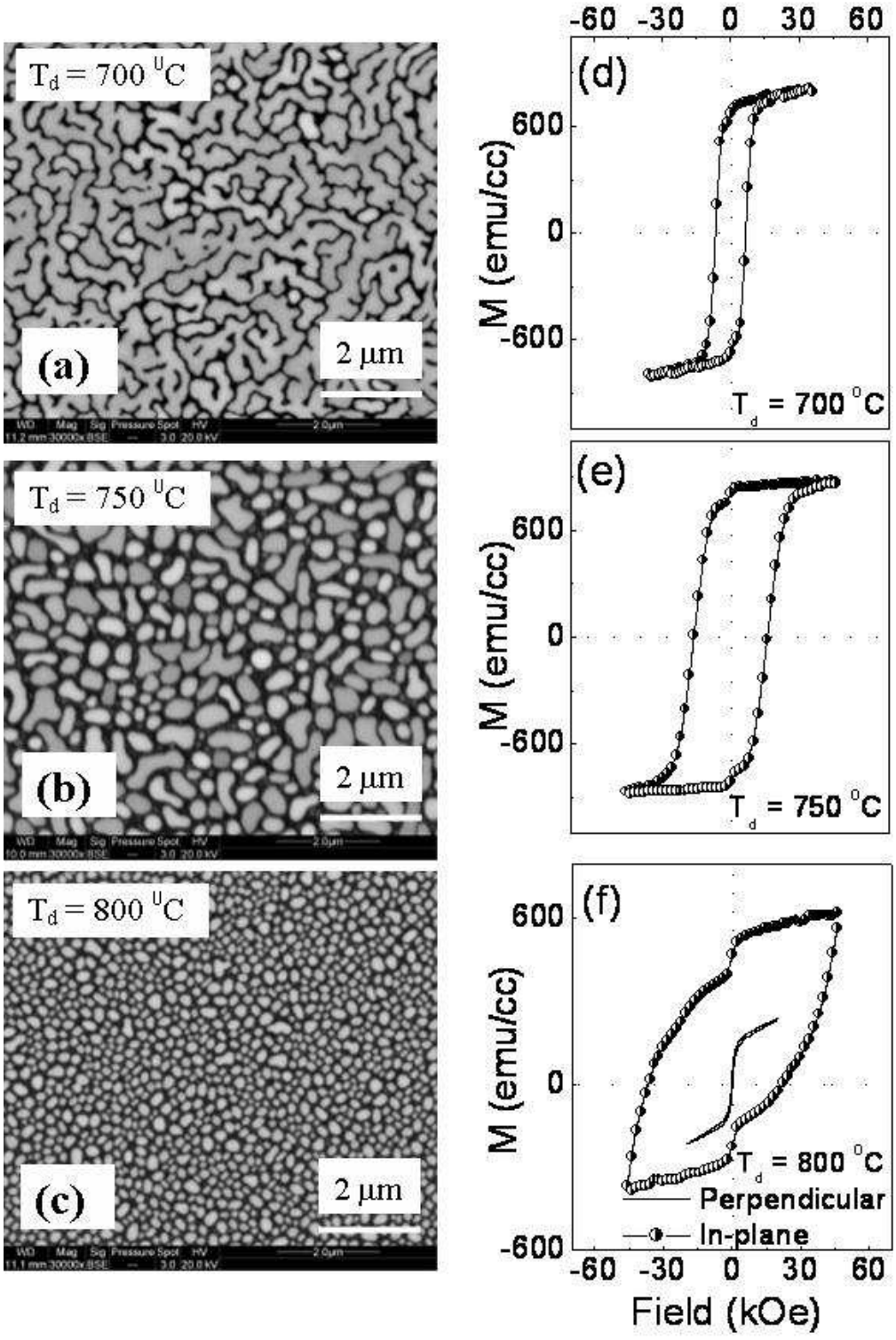
T_d = 700 °C
(a)
2 μm
T_d = 750 °C
(b)
2 μm
T_d = 800 °C
(c)
2 μm
(d)
(e)
(f)
M (emu/cc)
600
0
-600
-60 -30 0 30 60
T_d = 700 °C
T_d = 750 °C
T_d = 800 °C
Perpendicular
In-plane
Field (kOe)

FIG: 6

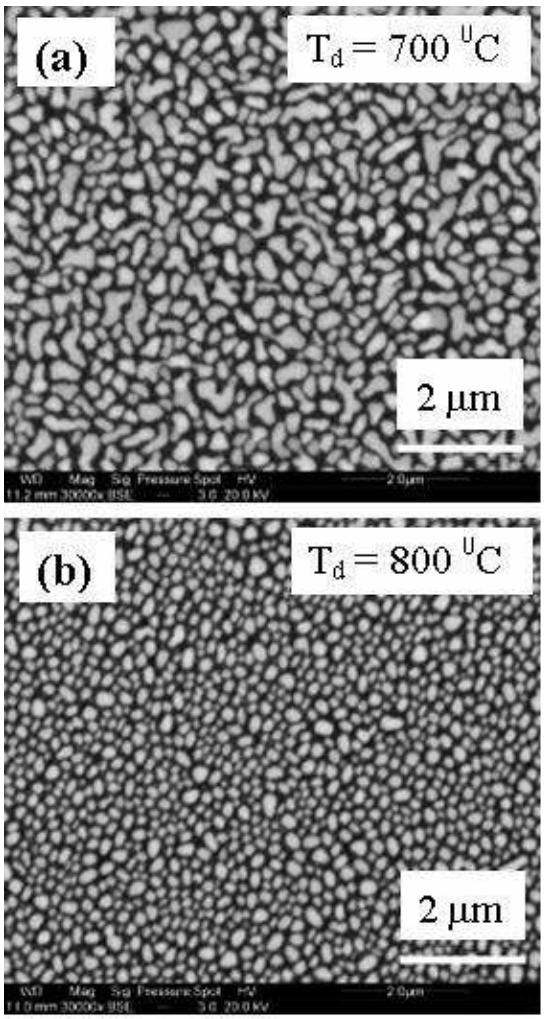

FIG: 7

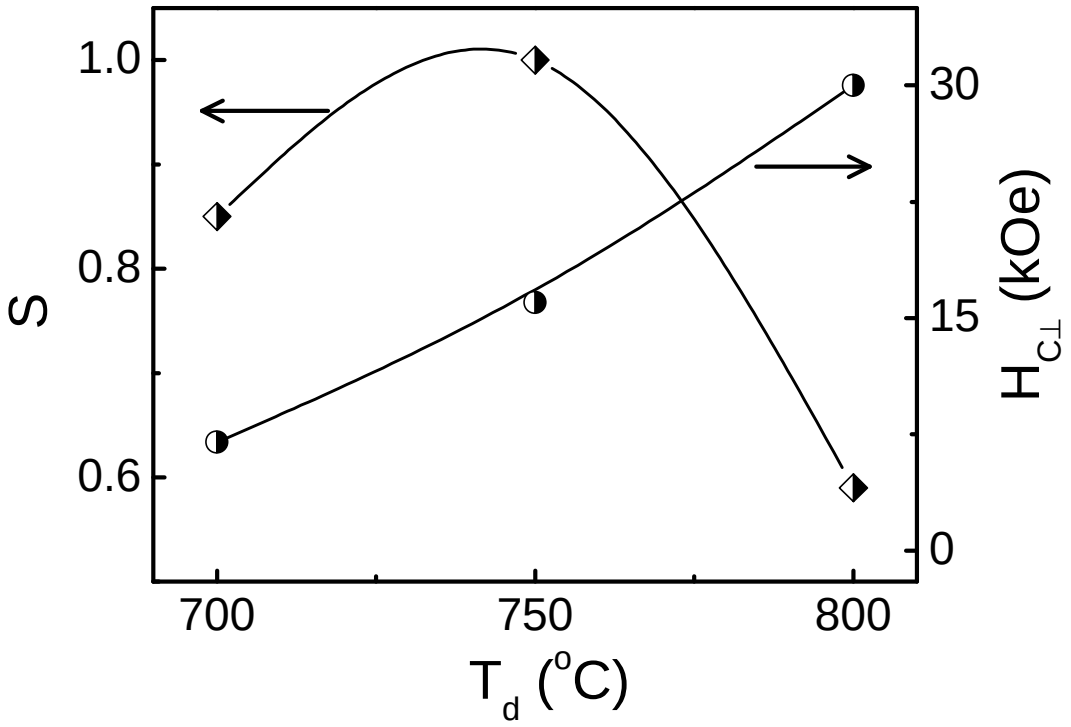

FIG: 8

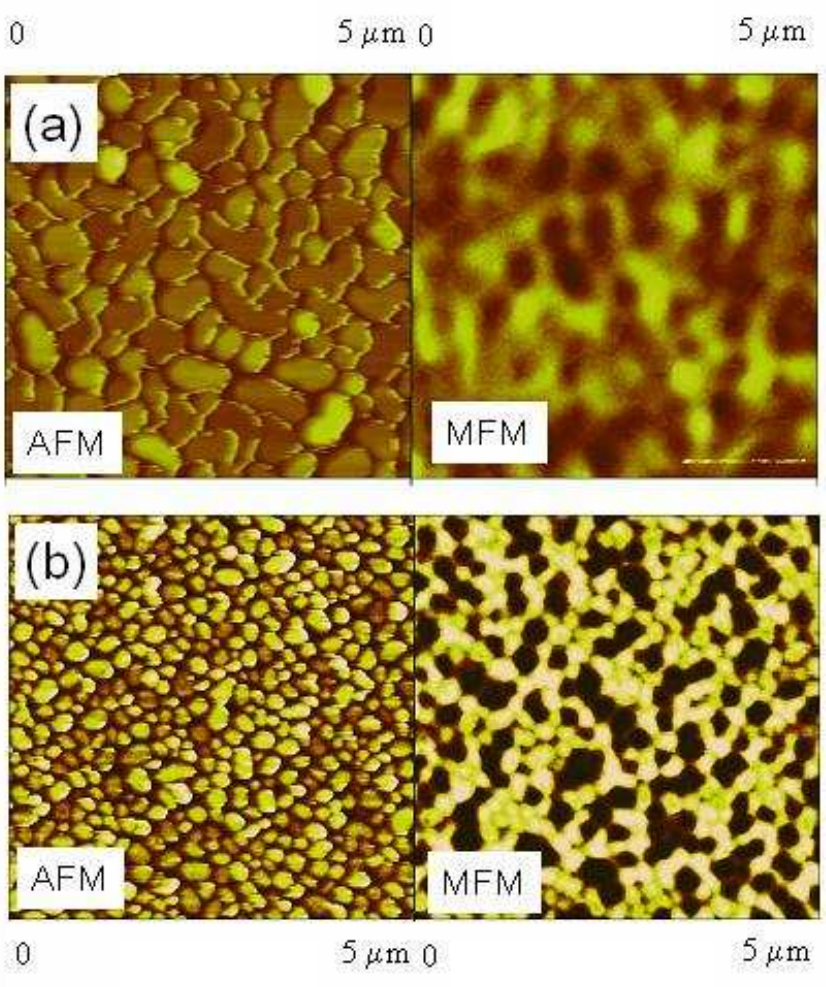

FIG: 9

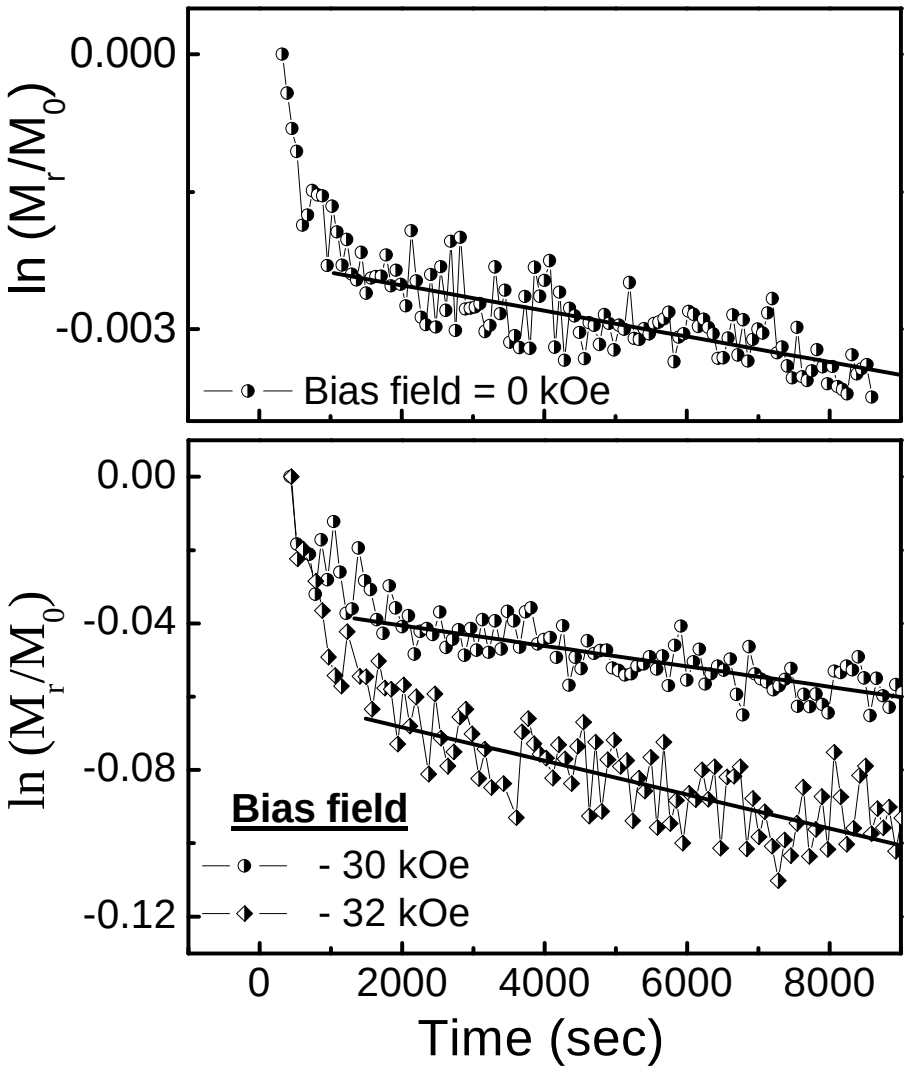
0.000
-0.003
ln (M_r/M_0)
Bias field = 0 kOe
0.00
-0.04
-0.08
-0.12
ln (M_r/M_0)
Bias field
- 30 kOe
- 32 kOe
0
2000
4000
6000
8000
Time (sec)

FIG: 10